Charge-Tunable Quantum Plasmons in Colloidal Semiconductor Nanocrystals

Alina M. Schimpf, Niket Thakkar, Carolyn E. Gunthardt, David J. Masiello,* and Daniel R. Gamelin*

Department of Chemistry, University of Washington, Seattle, Washington 98195-1700, United States

ABSTRACT Nanomaterials exhibiting plasmonic optical responses are impacting sensing, information processing, catalysis, solar, and photonics technologies. Recent advances have expanded the portfolio of plasmonic nanostructures into doped semiconductor nanocrystals, which allow dynamic manipulation of carrier densities. Once interpreted as intraband single-electron transitions, the infrared absorption of doped semiconductor nanocrystals is now commonly attributed to localized surface plasmon resonances and analyzed using the classical Drude model to determine carrier densities. Here, we show that the experimental plasmon resonance energies of photodoped ZnO nanocrystals with controlled sizes and carrier densities diverge from classical Drude model predictions at small sizes, revealing quantum plasmons in these nanocrystals. A Lorentz oscillator model more adequately describes the data and illustrates a closer link between plasmon resonances and single-electron transitions in semiconductors than in metals, highlighting a fundamental contrast between these two classes of plasmonic materials.

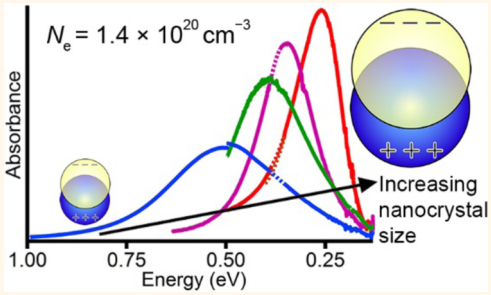

KEYWORDS: quantum dots · plasmons · doped nanocrystals · zinc oxide · photodoping

Carrier-doped semiconductor nanocrystals are envisioned as essential components of future information processing, solar energy conversion, and other technologies. Nanocrystal carrier doping generates new infrared (IR) absorption bands similar to localized surface plasmon resonances (LSPRs) of metal nanoparticles. Semiconductor nanocrystals showing such LSPRs have recently attracted broad attention,[1,2] in part because of the wide range of carrier densities achievable in such systems. Over just the past few years, LSPRs have been reported in many semiconductor nanocrystals with excess charge carriers introduced by aliovalent,[3−7] vacancy-induced,[8−10] or redox[11,12] doping. Central to any analysis of these LSPRs is an assessment of the carrier density. Many investigations have applied the classical Drude model to estimate carrier densities from IR absorption energies.[3−6,8,10−12] Others have assumed stoichiometric relationships between defects and carriers.[9] In semiconductor nanocrystals, however, a large fraction of aliovalent dopants or electronic defects can be compensated by localized surface charges,[13] and impurity doping of any type perturbs carrier wave functions.[14] Additionally, in some cases the carriers may be partially localized.[15] These factors complicate determination of carrier densities using the Drude model. Moreover, the Drude model itself may not even be adequate for semiconductor nanocrystals, which have much smaller carrier densities than metals, but this model has not been quantitatively tested. Finally, quantum confinement effects are not accounted for in the Drude model and have also not yet been investigated in LSPR-supporting semiconductors. Here, we analyze the IR absorption spectra of photodoped colloidal ZnO nanocrystals with tunable radii (r) and carrier densities (N_e) to assess the applicability of the Drude model in this case. These experimental data expose fundamental shortcomings of the Drude model when applied to semiconductor nanocrystals, revealing the existence of quantum plasmons in semiconductor nanocrystals and highlighting important contrasts between LSPRs in semiconductor and metal nanostructures.

Photodoped ZnO nanocrystals are among the best characterized carrier-doped colloidal semiconductor nanocrystals[13,16−23] and offer a unique platform for turning on, tuning, and investigating semiconductor

* Address correspondence to masiello@chem.washington.edu; gamelin@chem.washington.edu.

Received for review November 27, 2013 and accepted December 22, 2013.

Published online December 23, 2013
10.1021/nn406126u

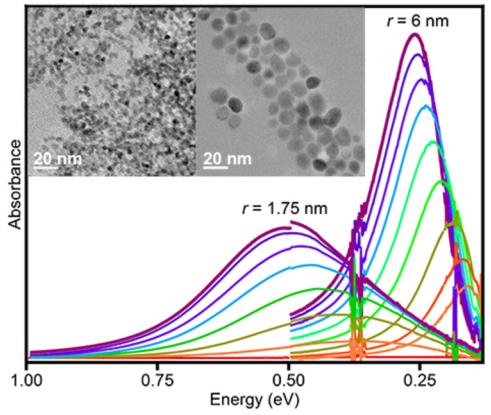

Figure 1. IR absorption spectra of r = 1.75 and 6 nm colloidal photodoped ZnO nanocrystals. For each sample, the increased IR absorption corresponds to progressively greater photodoping. Both samples display the same maximum photodoping level of $(1.4 \pm 0.4) \times 10^{20}$ cm^{-3}. This density corresponds to a maximum average occupancy of 3.2 ± 0.9 and 116 ± 22 electrons per nanocrystal for the small and large nanocrystals, respectively. Inset: TEM images of the r = 1.75 nm (left) and r = 6 nm (right) nanocrystals.

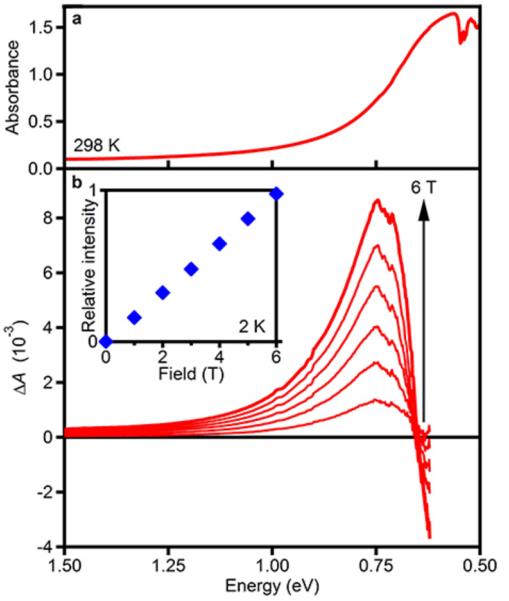

Figure 2. Room-temperature (a) absorption and (b) MCD spectra of heavily photodoped colloidal r = 1.55 nm ZnO nanocrystals. The arrow indicates increasing magnetic field strength in 1 T steps. The dip in panel (a) at ~0.55 eV is due to imperfect subtraction of solvent vibrations. Inset: Relative 2 K IR MCD intensities plotted as a function of magnetic field strength. The MCD spectra terminate at the instrumental limit of ~0.6 eV.

LSPRs. Anaerobic UV irradiation in the presence of an appropriate hole quencher allows accumulation of delocalized conduction-band electrons, achieving average carrier densities tunable from zero up to ~6×10^{20} cm^{-3}.[23] Unlike in other systems investigated to date, these carrier densities are readily determined by direct titration against mild redox reagents,[13,18,20,23,24] *providing a model-independent measure of this critical quantity*. Previous studies have described a new IR absorption band that accompanies the added conduction-band electrons,[17,19,20,25] but its interpretation remains ambiguous. It has generally been interpreted in terms of single-electron intra-conduction-band transitions,[17,19,20,25] but has recently also been interpreted in terms of LSPRs,[12] and similar IR absorption in Al^{3+}-doped ZnO nanocrystals has also been described as LSPRs.[26,27] If indeed this IR band is due to LSPRs, the relationship between these collective excitations and the anticipated single-electron excitations has yet to be revealed.

RESULTS AND ANALYSIS

Figure 1 shows IR absorption spectra of two anaerobic ZnO nanocrystal suspensions (r = 1.75 and 6 nm), each prepared and photodoped using ethanol for hole quenching as detailed previously (see Supporting Information for details).[23] Spectra collected at various UV irradiation times are shown, with increasing IR absorption reflecting increasing electron density.[19,20] The maximum photodoping corresponds to an electron density of $(1.4 \pm 0.4) \times 10^{20}$ cm^{-3} for both samples.[23] With added electrons, the IR absorption maxima blue shift while increasing in intensity. A similar blue shift has been reported in r = 2.1 nm ZnO nanocrystals,[19] where it was interpreted as arising from the increased energy spacings of intra-conduction-band single-electron transitions. The experimental shifts are slightly greater than predicted from tight-binding calculations,[19] but are comparable to expectations from the classical Drude model (Figure S4a). Similar shifts are observed in all sizes of nanocrystals (Figure S4b), even though the smallest have a maximum of ~3 conduction-band electrons, while the largest have up to ~130. This similarity suggests that the blue shift is correlated with electron *density* rather than number. Additionally, from tight-binding calculations,[19] a significant blue shift is not expected in large nanocrystals, where intraband spacings are nearly constant. Although it is conceivable that the blue shift reflects preferential reduction of larger nanocrystals, because intraband spacings are size-dependent and electrons can transfer rapidly from one nanocrystal to another,[14,21] the average radius (6 nm) for the larger ZnO nanocrystals of Figure 1 is well beyond the quantum confinement size regime (≤3.5 nm), allowing the conclusion that size heterogeneity is not responsible. On the basis of these considerations, the IR blue shift with increased photodoping is consistent with assignment of this IR band as an LSPR.

Magnetic circular dichroism (MCD) spectroscopy provides strong support for assignment of the IR band in photodoped ZnO nanocrystals as an LSPR. Figure 2 shows room-temperature absorption (a) and

variable-field MCD (b) spectra of photodoped r = 1.55 nm ZnO nanocrystals. The MCD intensity is very large ($|\Delta A/A_0| \approx 0.01$) but does not maximize at the absorption maximum, instead crossing zero close to the absorption maximum. The MCD intensity is temperature independent (Figure S5) and shows a linear dependence on magnetic field, even at 2 K (Figure 2, inset). Strikingly similar MCD data have been reported for the LSPRs of colloidal Au nanoparticles,[28] which also show very large ($|\Delta A/A_0| \approx 0.001$) and temperature-independent derivative-shaped MCD intensities. These similarities support the assignment of the ZnO IR peak as an LSPR.

Temperature-independent derivative-like band shapes are typically characteristic of *A*-term MCD intensities,[29] which derive from the effects of magnetic fields on excited states rather than from magnetization of the ground state (*C*-term).[29] Previous MCD spectra of plasmons in Au nanoparticles have been interpreted in this way.[28] For the photodoped ZnO nanocrystals, this interpretation is surprising because of the strong correlation between IR absorption and the ground-state g = 1.96 electron paramagnetic resonance (EPR) intensity from the delocalized electrons within these nanocrystals.[20,30] Paramagnets typically display *C*-term MCD intensity that increases rapidly with decreasing temperature (in proportion to $1/T$ for simple Curie-type paramagnets; see Figure S6) and therefore dominates at low temperatures. The MCD of these photodoped ZnO nanocrystals is thus not typical of paramagnetic chromophores. We propose that the temperature independence of the plasmon MCD intensities in these nanocrystals may alternatively reflect Pauli-type paramagnetism, a characteristic of conduction electrons in most nonferromagnetic metals.[31]

Several samples of colloidal ZnO nanocrystals were prepared with average radii ranging from 1.75 to 6 nm and all photodoped to the same independently verified electron density of $(1.4 \pm 0.4) \times 10^{20}$ cm^{-3}.[23] Figure 3a shows IR absorption spectra of these nanocrystals and illustrates a key result of this study: At a constant carrier density, the IR absorption blue shifts substantially with decreasing nanocrystal radius. Figure 3b plots the energies of the absorption maxima as a function of nanocrystal radius (blue circles). For large radii ($\gtrsim$5 nm), this energy approaches an asymptote of ~0.25 eV, agreeing well with the LSPR energies of ZnO thin films[32] (which should be greater by a factor of ~1.2). This size dependence is very similar to that observed for the first excitonic absorption maximum in ZnO nanocrystals arising from quantum confinement,[33] but it is qualitatively different from that anticipated by the classical Drude model.

The LSPR frequencies predicted by the classical Drude model are given by

$$\omega_{sp}^{Drude} = \sqrt{\frac{N_e e^2}{\varepsilon_0 m_e(\varepsilon_\infty + 2\varepsilon_m)} - \gamma^2} \qquad (1)$$

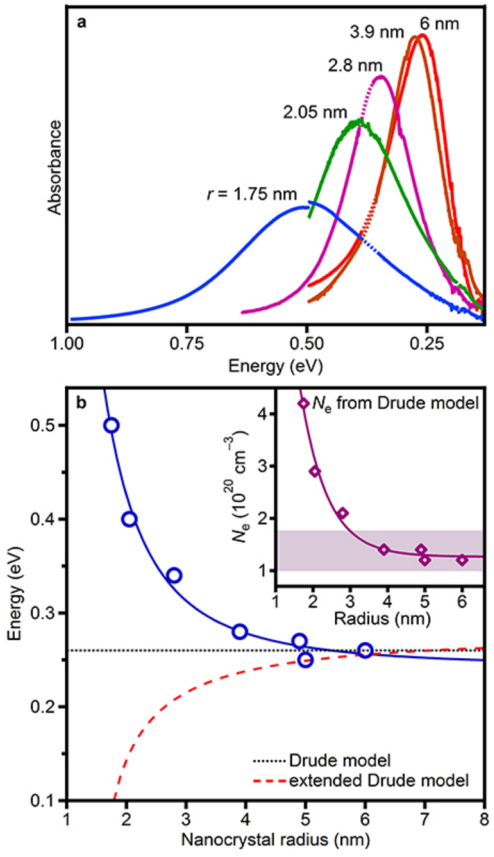

Figure 3. (a) IR absorption spectra of a series of colloidal ZnO nanocrystals with different radii, each photodoped to an average carrer density of $N_e = (1.4 \pm 0.4) \times 10^{20}$ cm^{-3}. Dotted lines indicate the region of intense C−H stretches. (b) IR peak maxima *versus* nanocrystal radius (blue circles). The dotted black line shows the Drude model (eq 1) prediction for LSPR energies at $N_e = (1.4 \pm 0.4) \times 10^{20}$ cm^{-3}. The dashed red line extends this model to account for increased surface scattering in small nanocrystals (eq 2). Inset: Predicted (diamonds, from eq 1) and experimental (shaded region) carrier densities plotted *versus* nanocrystal radius. Solid lines are guides to the eye.

This relationship has been widely employed in the analysis of heavily doped semiconductor nanocrystals. Here, $\gamma = \gamma_{bulk}$ is the bulk scattering frequency, e is the elementary charge, ε_0 is the permittivity of vacuum, ε_m is the medium dielectric (estimated as 2.25 for toluene), ε_∞ is the high-frequency dielectric (3.72 for ZnO),[34] and $m_e = 0.28m_0$ is the mass of an electron in ZnO.[34] Application of eq 1 to predict the LSPR frequencies of ZnO nanocrystals photodoped to $N_e = 1.4 \times 10^{20}$ cm^{-3} yields the dotted line in Figure 3b. The Drude model accurately estimates ω_{sp} for the largest ZnO nanocrystals but fails for smaller nanocrystals. Equivalently, the inset of Figure 3b compares the experimental carrier densities (shaded) with those estimated from eq 1. Here, N_e values were calculated from the IR absorption using ω_{sp} and γ as the maxima and half-widths-at-half-maxima (hwhm), respectively. The Drude model accurately estimates the carrier density of the largest ZnO nanocrystals, yielding a value of 1.2×10^{20} cm^{-3}, but it

predicts a carrier density roughly 4 times too large (4.2×10^{20} cm^{-3}) for the smallest nanocrystals. Furthermore, an extended Drude model that accounts for size-dependent surface scattering through modification of the scattering frequency,

$$\gamma = \gamma_{bulk} + \frac{A\nu_F}{r} \quad (2)$$

actually predicts an absorption *red shift* with decreasing radius for a constant N_e (Figure 3b, dashed line). Here, ν_F is the Fermi velocity (8.4×10^5 m/s in ZnO)[35] and A is an empirical constant whose value is debated in the literature.[36] Drude models thus fail to describe the IR absorption spectra of carrier-doped ZnO quantum dots. For accurate interpretation of this IR absorption, a more sophisticated model is needed.

To address these shortcomings, we introduce a quantum mechanical correction to the driving force on a classical Lorentz electron in an external electric field.[37] A similar semiclassical approach was recently used to model a blue shift of Ag nanoparticle LSPR energies with decreasing radius.[38] We model electron motion within a spherical semiconductor nanocrystal as a collection of damped and driven harmonic oscillators, where the driving force is dependent on both the incident electric field and quantum mechanical responses to the boundary. Quantum confinement also alters the harmonic restoring force by discretizing the set of available transition frequencies, ω_{if}, where i and f are composite labels for initial and final quantum states. This model yields the dielectric function

$$\varepsilon(\omega) = \varepsilon_{IB}(\omega) - \omega_p{}^2 \sum_{i,f} \frac{S_{if}}{\omega^2 + i\gamma\omega - \omega_{if}{}^2} \quad (3)$$

where $\omega_p = (N_e e^2/\varepsilon_0 m_e)^{1/2}$ is the bulk plasma frequency, S_{if} is the oscillator strength obeying the Thomas–Reiche–Kuhn sum rule, γ is the size-dependent scattering frequency (eq 2), and $\varepsilon_{IB}(\omega)$ represents contributions from interband transitions.

To apply this dielectric function to photodoped ZnO nanocrystals, conduction electrons are modeled as noninteracting particles within an infinite spherical potential well. The quasi-spherical shapes of our nanocrystals are verified by transmission electron microscopy (Figure 1, inset). The many-electron character is introduced by imposing the Pauli exclusion principle and a hydrogenic shell-filling scheme with degeneracy $2n^2$ for each principle quantum number, n. Under these assumptions, the Fermi level, n_F, is determined by finding the nearest integer to the solution of

$$n_e = \sum_{n=1}^{n_F} 2n^2 \quad (4)$$

where $n_e = (4/3)\pi r^3 N_e$ is the total number of conduction electrons. Dominant contributions to the sum in eq 3 come from low-energy excitations around this value of n_F (see Supporting Information). Finally, interband transitions in ZnO occur above ~3.5 eV, far from the IR region. Therefore, it suffices to replace $\varepsilon_{IB}(\omega)$ with ε_∞ to impose consistency with the behavior of bulk ZnO. With this approach, LSPRs are found according to the Clausius–Mossotti relation at frequencies where

$$\mathrm{Re}[\varepsilon(\omega_{sp})] = -2\varepsilon_m \quad (5)$$

Only frequencies in normal dispersion regimes ($(\partial/\partial\omega)\mathrm{Re}[\varepsilon(\omega)] > 0$) are considered. All calculations use the experimental carrier density of 1.4×10^{20} cm^{-3}.

Figure 4a presents the spectral dependence of the real part of the ZnO dielectric function for various nanocrystal sizes (see Figure S7 for the imaginary parts). The corresponding normalized absorption efficiencies are shown in Figure 4b. LSPR energies, $\hbar\omega_{sp}$, were determined according to eq 5 and are plotted on top of the absorption efficiencies (black circles). The single-electron transition energies, $\hbar\omega_{if}$, are also plotted in Figure 4b (white circles), with symbol opacities proportional to S_{if}. Only LSPRs are found in regions of high absorption efficiency, supporting the conclusion that plasmons dominate the ZnO nanocrystal IR absorption spectra at these experimental carrier densities. The single-electron transitions are relatively weak at these high carrier densities because they involve only one electron, whereas the plasmon excitations involve many. As the radius decreases, the LSPR and lowest-energy single-electron transition energies converge. A similar convergence occurs for fixed radius as N_e is reduced (Figure S7). The discontinuities in these calculations, which appear as jumps in Figure 4b, are a consequence of the shell-filling approximation used in our model (eq 4).

As observed experimentally, the calculated results of Figure 4b show an increase in $\hbar\omega_{sp}$ with decreasing radius, starting from bulk. We conclude that this model, although idealized and without any adjustable parameters, successfully captures the essence of the experimental observations. The calculated size dependence is steeper than observed experimentally, possibly because of the model's inability to account for electron tunneling beyond the nanocrystal surface ("spill-out").[39] Tunneling makes the smallest nanocrystals effectively larger and weakens the size dependence. Another factor could be the existence of delocalized surface states, such as Shockley or Tamm states.[40] Surface states could be important at high electron densities, particularly if the electron-charge-compensating protons from photodoping all reside at the ZnO nanocrystal surfaces. Confinement of such surface states is documented in metals, where electrons behave as particles in two-dimensional boxes.[41] The calculations of Figure 4 are based on an idealized model and do not account for surface states. We note that the experimental size dependence of the IR absorption is similar at both high and low electron

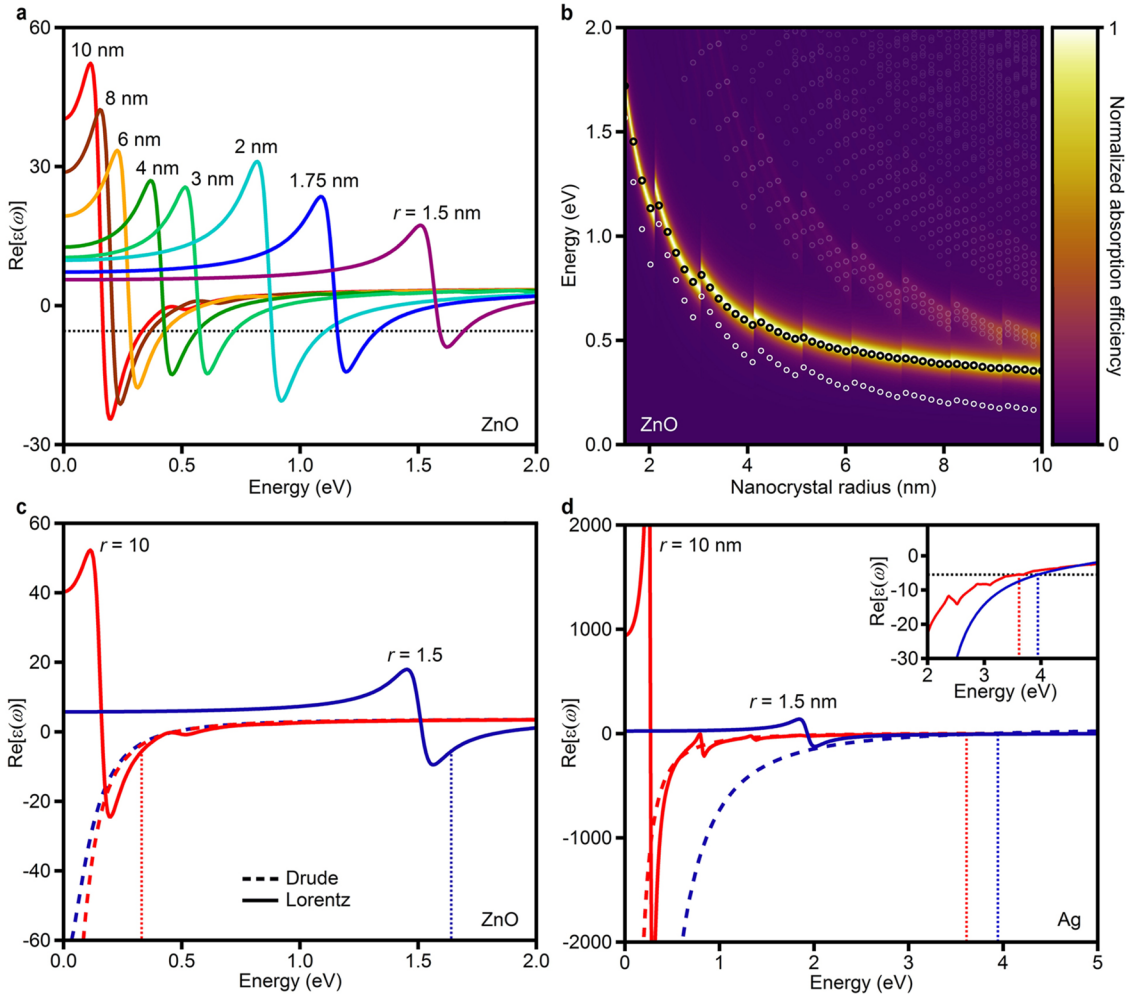

Figure 4. Spectral dependence of (a) the real part of the ZnO dielectric function for various nanocrystal radii and of (b) the corresponding normalized absorption efficiencies as a function of nanocrystal radius. The dotted black line in panel (a) is positioned at $-2\varepsilon_m$. The crossings of this line with Re[$\varepsilon(\omega)$] in regions of normal dispersion correspond to LSPR energies, $\hbar\omega_{sp}$, which are displayed as black open circles in panel (b). The white circles in panel (b) correspond to single-electron transitions, and their opacities are scaled to their oscillator strengths. Also shown are the spectral dependencies of the real part of the dielectric functions for (c) ZnO and (d) Ag calculated with the Drude (dashed lines) and Lorentz (solid lines) models for two different sizes. The dotted vertical lines indicate the crossings of the Lorentz model with $-2\varepsilon_m = -5.5$ for the two different sizes (red and blue). All ZnO calculations use the experimental carrier density of 1.4×10^{20} cm^{-3}.

densities (Figure S4b), arguing against major contributions from surface states. Additional deviations from ideality may arise from nanocrystal shape anisotropies, surface ligation, and changes in the local dielectric function at the nanocrystal surface. Expansion of the model to include adjustable parameters accounting for such effects can indeed improve quantitative agreement with the experimental data (*e.g.*, Figure S8), but it does not provide greater insight into the physical problem. Overall, the data in Figure 3b reveal large quantum size effects manifested in the LSPRs of doped semiconductor nanocrystals. *This result constitutes the first experimental demonstration of quantum confinement effects on LSPRs in semiconductors.* We stress that this size dependence is identified only because carrier densities could be measured independently. Application of the Drude model to deduce carrier densities would have yielded a qualitatively different understanding of these semiconductor LSPRs.

It is interesting to note that, unlike in metals, LSPRs in photodoped ZnO nanocrystals occur spectrally near the regions of large anomalous dispersion (Figure 4c), placing them close to the most allowed single-electron transitions. In this regime, the Lorentz dielectric model is strongly non-Drude in character, and the free-electron picture used for metallic plasmons is qualitatively incorrect. Instead, the ZnO LSPRs become very sensitive to the most-dominant single-electron transitions and converge to their energies in the limit of low carrier occupancy. Moreover, because this spectral proximity is a result of the relatively low carrier densities, it is not specific to ZnO or to nanocrystals. Carrier densities achievable in semiconductors are generally 2−3 orders of magnitude smaller than in metals, making this relationship between LSPRs and single-electron transitions universally significant. Figure 4c and d highlight this important contrast, comparing the

calculated dielectric functions of photodoped ZnO nanocrystals and Ag nanoparticles at two radii. Because of its high carrier density, collective excitations in Ag occur far from the dominant single-electron transitions, within the free-electron (Drude) part of the Lorentz dielectric function. Consequently, they are spectrally distant from and relatively insensitive to the most-allowed single-electron transitions (Figure S9). In stark contrast, the lower carrier densities of photodoped ZnO nanocrystals link the plasmons to dominant single-electron excitations, making them difficult to distinguish energetically. When these single-electron transitions shift due to changing nanocrystal radius, the collective excitations follow. These insights reconcile conflicting evidence for interpretation of the IR bands of doped semiconductor nanocrystals as plasmon resonances *versus* single-electron excitations.

CONCLUSION

In summary, carrier-doped semiconductor nanocrystals offer a unique platform for tuning plasmons on nanometer length scales. The ability to control and quantify carrier densities in colloidal ZnO nanocrystals has allowed experimental assessment of the classical Drude model commonly applied to interpret IR absorption spectra of doped semiconductor nanocrystals. Investigating the relationship between nanocrystal size and IR absorption energy at constant carrier density has revealed that the Drude model fails for small nanocrystals in which electron wave functions are quantum confined. A Lorentz oscillator model that accounts for quantum-mechanical corrections qualitatively reproduces the experimental size dependence. Both the experimental and theoretical results bridge the single-electron and LSPR regimes, displaying quantum confinement in small nanocrystals and converging to classical bulk LSPRs in large nanocrystals. These findings shed new light on semiconductor plasmonics, with important ramifications for both fundamental investigations of doped semiconductor nanocrystals and future applications of this emerging class of materials.

METHODS

Colloidal ZnO nanocrystals were synthesized by base-initiated hydrolysis and condensation as described in detail previously.[42,43] Dropwise addition of 22 mmol of tetramethylammonium hydroxide pentahydrate dissolved in 40 mL of EtOH to 13 mmol of zinc acetate dihydrate in 135 mL of dimethylsulfoxide at room temperature leads to nanocrystal nucleation and growth. After appropriate growth times, the reaction is stopped by precipitation with ~300 mL of ethyl acetate, and the nanocrystals are centrifuged, resuspended in EtOH, and precipitated with heptane. To suspend the nanocrystals in nonpolar solvents, the surface ligands are exchanged by adding dodecylamine (DDA) heated to above its melting point (29 °C). The DDA-capped nanocrystals are precipitated with EtOH and collected by centrifugation, and their ligands exchanged by heating in 90% trioctylphosphine oxide (TOPO) at ~100 °C for 30 min. These nanocrystals are then washed/resuspended with EtOH/toluene as described above. To achieve the largest radii, the nanocrystals are left in DDA at 180 °C under N_2 for 0.5−24 h prior to TOPO ligand exchange. For small nanocrystals (r < 3.2 nm), radii were estimated from their UV electronic absorption spectra using established empirical relationships.[33] For larger nanocrystals, radii were estimated from pXRD line widths and by statistical analysis of TEM images. All nanocrystals used in this study were roughly spherical, with more deviation from spherical shape in the larger nanocrystals (see Supporting Information). ZnO nanocrystal concentrations were determined analytically. Briefly, 200 μL of the nanocrystal suspension was dried and digested in 400 μL of ultrapure nitric acid (TraceSELECT, Fluka). The resulting solution was diluted with a known amount of ultrapure water (~10.00 g, measured to two decimal places on a balance), and the Zn^{2+} concentration measured using inductively coupled plasma atomic emission spectroscopy (Perkin-Elmer 8300). The nanocrystal concentration was then calculated using the known dilution factors and nanocrystal radii to convert from Zn^{2+} concentration to nanocrystal concentration.

For infrared absorption measurements on photodoped nanocrystals, nanocrystal solutions were prepared anaerobically to be ~0.15 M Zn^{2+} in toluene. These solutions were loaded into an air-free IR cell in an inert-atmosphere glovebox, which was then removed from the glovebox for subsequent experiments. The nanocrystals were photodoped by placing the IR cell in front of a 100 W Hg/Xe Oriel photolysis lamp for short times (1−20 s between spectra). The IR absorption was monitored during photodoping until it stopped increasing. Residual EtOH from the synthesis and purification procedures is the hole quencher.[22]

For MCD measurements, a 200 μL sample of nanocrystals was prepared anaerobically in 2-methyltetrahydrofuran, and to it was added 2 μL of 1 M Li[Et_3BH], which serves as a hole quencher.[23] The sample was prepared in the glovebox by dropping a small amount of this solution onto a polished quartz disc holding a Teflon spacer and placing another quartz disc on top. These nanocrystals were photodoped as described above and placed into the magneto-cryostat.

Electron densities in photodoped ZnO nanocrystals have been determined *via* titration against a mild oxidant, [$FeCp^*_2$]-[BAr_F].[13,18,20,23,24] Aliquots of [$FeCp^*_2$][BAr_F] were added to photodoped ZnO nanocrystals under anaerobic conditions, and electron transfer from the photodoped ZnO nanocrystals to $[FeCp^*_2]^+$ was followed spectroscopically to determine the average number of electrons per nanocrystal and, hence, the electron density. Further details are provided in the Supporting Information.

UV/visible/near-IR absorption spectra were collected using a Cary 500 spectrometer. pXRD data were collected using a Bruker D8 Discover diffractometer. TEM images were collected using a FEI Tecnai G2 F20. MCD spectra were measured using an Aviv 40DS spectropolarimeter with an InGaAs detector (Teledyne-Judson), with samples mounted in a high-field superconducting magneto-optical cryostat (Cryo-Industries SMC-1659 OVT) with a variable-temperature sample compartment oriented in the Faraday configuration.

Conflict of Interest: The authors declare no competing financial interest.

Acknowledgment. The authors thank Prof. Alexander Govorov for valuable discussions. This work was supported by the U.S. National Science Foundation (Graduate Research Fellowship DGE-1256082 to A.M.S. and N.T., CAREER Award CHE-1253775 to D.J.M., and DMR-1206221 to D.R.G.). This work was funded partially by a Washington NASA Space Grant Consortium Summer Undergraduate Research Fellowship to C.E.G. Part of this work was conducted at the University of Washington NanoTech User Facility, a member of the NSF National Nanotechnology Infrastructure Network.

Supporting Information Available: Detailed methods of electron density determination, plots of LSPR energy as a function of electron density, additional MCD spectra and calculated field/temperature dependence, additional details for the theoretical model, real and imaginary parts of the Lorentz dielectric function, plot of calculated energy shift with increasing electron density, and absorption efficiency as a function of size and energy for Ag nanoparticles. This material is available free of charge *via* the Internet at http://pubs.acs.org.

REFERENCES AND NOTES

1. Routzahn, A. L.; White, S. L.; Fong, L.-K.; Jain, P. K. Plasmonics with Doped Quantum Dots. *Isr. J. Chem.* **2012**, *52*, 983–991.
2. Scotognella, F.; Valle, G.; Srimath Kandada, A.; Zavelani-Rossi, M.; Longhi, S.; Lanzani, G.; Tassone, F. Plasmonics in Heavily-Doped Semiconductor Nanocrystals. *Eur. Phys. J. B* **2013**, *86*, 1–13.
3. Nütz, T.; zum Felde, U.; Haase, M. Wet-Chemical Synthesis of Doped Nanoparticles: Blue-Colored Colloids of *n*-Doped SnO_2:Sb. *J. Chem. Phys.* **1999**, *110*, 12142–12150.
4. Wang, T.; Radovanovic, P. V. Free Electron Concentration in Colloidal Indium Tin Oxide Nanocrystals Determined by Their Size and Structure. *J. Phys. Chem. C* **2011**, *115*, 406–413.
5. Niezgoda, J. S.; Harrison, M. A.; McBride, J. R.; Rosenthal, S. J. Novel Synthesis of Chalcopyrite $Cu_xIn_yS_2$ Quantum Dots with Tunable Localized Surface Plasmon Resonances. *Chem. Mater.* **2012**, *24*, 3294–3297.
6. Chou, L. W.; Shin, N.; Sivaram, S. V.; Filler, M. A. Tunable Mid-Infrared Localized Surface Plasmon Resonances in Silicon Nanowires. *J. Am. Chem. Soc.* **2012**, *134*, 16155–16158.
7. De Trizio, L.; Buonsanti, R.; Schimpf, A. M.; Llordes, A.; Gamelin, D. R.; Simonutti, R.; Milliron, D. J. Nb-Doped Colloidal TiO_2 Nanocrystals with Tunable Infrared Absorption. *Chem. Mater.* **2013**, *25*, 3383–3390.
8. Luther, J.; Jain, P.; Ewers, T.; Alivisatos, A. Localized Surface Plasmon Resonances Arising from Free Carriers in Doped Quantum Dots. *Nat. Mater.* **2011**, *10*, 361–366.
9. Manthiram, K.; Alivisatos, A. Tunable Localized Surface Plasmon Resonances in Tungsten Oxide Nanocrystals. *J. Am. Chem. Soc.* **2012**, *134*, 3995–3998.
10. Polking, M. J.; Jain, P. K.; Bekenstein, Y.; Banin, U.; Millo, O.; Ramesh, R.; Alivisatos, A. P. Controlling Localized Surface Plasmon Resonances in GeTe Nanoparticles Using an Amorphous-to-Crystalline Phase Transition. *Phys. Rev. Lett.* **2013**, *111*, 037401.
11. Palomaki, P. K. B.; Miller, E. M.; Neale, N. R. Control of Plasmonic and Interband Transitions in Colloidal Indium Nitride Nanocrystals. *J. Am. Chem. Soc.* **2013**, *135*, 14142–14150.
12. Faucheaux, J. A.; Jain, P. K. Plasmons in Photocharged ZnO Nanocrystals Revealing the Nature of Charge Dynamics. *J. Phys. Chem. Lett.* **2013**, *4*, 3024–3030.
13. Schimpf, A. M.; Ochsenbein, S. T.; Buonsanti, R.; Milliron, D. J.; Gamelin, D. R. Comparison of Extra Electrons in Colloidal *n*-type Al^{3+}-Doped and Photochemically Reduced ZnO Nanocrystals. *Chem. Commun.* **2012**, *48*, 9352–9354.
14. Cohn, A. W.; Kittilstved, K. R.; Gamelin, D. R. Tuning the Potentials of "Extra" Electrons in Colloidal n-Type ZnO Nanocrystals via Mg^{2+} Substitution. *J. Am. Chem. Soc.* **2012**, *134*, 7937–7943.
15. Kriegel, I.; Rodríguez-Fernández, J.; Wisnet, A.; Zhang, H.; Waurisch, C.; Eychmüller, A.; Dubavik, A.; Govorov, A. O.; Feldmann, J. Shedding Light on Vacancy-Doped Copper Chalcogenides: Shape-Controlled Synthesis, Optical Properties, and Modeling of Copper Telluride Nanocrystals with Near-Infrared Plasmon Resonances. *ACS Nano* **2013**, *7*, 4367–4377.
16. Haase, M.; Weller, H.; Henglein, A. Photochemistry and Radiation Chemistry of Colloidal Semiconductors. 23. Electron Storage on ZnO Particles and Size Quantization. *J. Phys. Chem.* **1988**, *92*, 482–487.
17. Shim, M.; Guyot-Sionnest, P. Organic-Capped ZnO Nanocrystals: Synthesis and *n*-Type Character. *J. Am. Chem. Soc.* **2001**, *123*, 11651–11654.
18. Wood, A.; Giersig, M.; Mulvaney, P. Fermi Level Equilibration in Quantum Dot-Metal Nanojunctions. *J. Phys. Chem. B* **2001**, *105*, 8810–8815.
19. Germeau, A.; Roest, A. L.; Vanmaekelbergh, D.; Allan, G.; Delerue, C.; Meulenkamp, E. A. Optical Transitions in Artificial Few-Electron Atoms Strongly Confined Inside ZnO Nanocrystals. *Phys. Rev. Lett.* **2003**, *90*, 097401.
20. Liu, W. K.; Whitaker, K. M.; Smith, A. L.; Kittilstved, K. R.; Robinson, B. H.; Gamelin, D. R. Room-Temperature Electron Spin Dynamics in Free-Standing ZnO Quantum Dots. *Phys. Rev. Lett.* **2007**, *98*, 186804.
21. Hayoun, R.; Whitaker, K. M.; Gamelin, D. R.; Mayer, J. M. Electron Transfer between Colloidal ZnO Nanocrystals. *J. Am. Chem. Soc.* **2011**, *133*, 4228–4231.
22. Cohn, A. W.; Janßen, N.; Mayer, J. M.; Gamelin, D. R. Photocharging ZnO Nanocrystals: Picosecond Hole Capture, Electron Accumulation, and Auger Recombination. *J. Phys. Chem. C* **2012**, *116*, 20633–20642.
23. Schimpf, A. M.; Gunthardt, C. E.; Rinehart, J. D.; Mayer, J. M.; Gamelin, D. R. Controlling Carrier Densities in Photochemically Reduced Colloidal ZnO Nanocrystals: Size Dependence and Role of the Hole Quencher. *J. Am. Chem. Soc.* **2013**, *135*, 16569–16577.
24. Schrauben, J.; Hayoun, R.; Valdez, C.; Braten, M.; Fridley, L.; Mayer, J. Titanium and Zinc Oxide Nanoparticles Are Proton-Coupled Electron Transfer Agents. *Science* **2012**, *336*, 1298–1599.
25. Shim, M.; Guyot-Sionnest, P. n-Type Colloidal Semiconductor Nanocrystals. *Nature* **2000**, *407*, 981–983.
26. Buonsanti, R.; Llordes, A.; Aloni, S.; Helms, B.; Milliron, D. Tunable Infrared Absorption and Visible Transparency of Colloidal Aluminum-Doped Zinc Oxide Nanocrystals. *Nano Lett.* **2011**, *11*, 4706–4716.
27. Garcia, G.; Buonsanti, R.; Llordes, A.; Runnerstrom, E. L.; Bergerud, A.; Milliron, D. J. Near-Infrared Spectrally Selective Plasmonic ElectrochromicThin Films. *Adv. Opt. Mater.* **2013**, *1*, 215–220.
28. Zaitoun, M. A.; Mason, W. R.; Lin, C. T. Magnetic Circular Dichroism Spectra for Colloidal Gold Nanoparticles in Xerogels at 5.5 K. *J. Phys. Chem. B* **2001**, *105*, 6780–6784.
29. Piepho, S. B.; Schatz, P. N. *Group Theory in Spectroscopy with Applications to Magnetic Circular Dichroism*; Wiley: New York, USA, 1983.
30. Whitaker, K. M.; Ochsenbein, S. T.; Polinger, V. Z.; Gamelin, D. R. Electron Confinement Effects in the EPR Spectra of Colloidal n-Type ZnO Quantum Dots. *J. Phys. Chem. C* **2008**, *112*, 14331–14335.
31. Kondo, J. *The Physics of Dilute Magnetic Alloys*; Cambridge University Press: United Kingdom, 2012.
32. Sachet, E.; Losego, M. D.; Guske, J.; Franzen, S.; Maria, J. P. Mid-Infrared Surface Plasmon Resonance in Zinc Oxide Semiconductor Thin Films. *Appl. Phys. Lett.* **2013**, *102*, 051111.
33. Wood, A.; Giersig, M.; Hilgendorff, M.; Vilas-Campos, A.; Liz-Marzán, L. M.; Mulvaney, P. Size Effects in ZnO: The Cluster to Quantum Dot Transition. *Aust. J. Chem.* **2003**, *56*, 1051–1057.
34. Madelung, O. *Semiconductors: Data Handbook*; Springer: New York, 2004.
35. Behera, H.; Mukhopadhyay, G. Strain-Tunable Band Parameters of ZnO Monolayer in Graphene-Like Honeycomb Structure. *Phys. Lett. A* **2012**, *376*, 3287–3289.
36. Kreibig, U.; Genzel, L. Optical Absorption of Small Metallic Particles. *Surf. Sci.* **1985**, *156*, 678–700.
37. Dressel, M.; Grüner, G. *Electrodynamics of Solids*; Cambridge University Press: United Kingdom, 2002.
38. Scholl, J. A.; Koh, A. L.; Dionne, J. A. Quantum Plasmon Resonances of Individual Metallic Nanoparticles. *Nature* **2012**, *483*, 421–427.
39. Monreal, R. C.; Antosiewicz, T. J.; Apell, S. P. Competition between Surface Screening and Size Quantization for Surface Plasmons in Nanoparticles. *New J. Phys.* **2013**, *15*, 083044.

40. Shockley, W. On the Surface States Associated with a Periodic Potential. *Phys. Rev.* **1939**, *56*, 317–323.
41. Crommie, M. F.; Lutz, C. P.; Eigler, D. M. Confinement of Electrons to Quantum Corrals on a Metal Surface. *Science* **1993**, *262*, 218–220.
42. Schwartz, D. A.; Norberg, N. S.; Nguyen, Q. P.; Parker, J. M.; Gamelin, D. R. Magnetic Quantum Dots: Synthesis, Spectroscopy, and Magnetism of Co^{2+}- and Ni^{2+}-Doped ZnO Nanocrystals. *J. Am. Chem. Soc.* **2003**, *125*, 13205–13218.
43. Norberg, N. S.; Gamelin, D. R. Influence of Surface Modification on the Luminescence of Colloidal ZnO Nanocrystals. *J. Phys. Chem. B* **2005**, *109*, 20810–20816.